The effect of strontium and barium doping on perovskite-structured energy materials for photovoltaic applications

Ming-Chung Wu [a,b,c,*], Wei-Cheng Chen [a], Shun-Hsiang Chan [a], Wei-Fang Su [d]

a Department of Chemical and Materials Engineering, Chang Gung University, Taoyuan 33302, Taiwan
b Center for Reliability Sciences & Technologies, Chang Gung University, Taoyuan 33302, Taiwan
c Division of Neonatology, Department of Pediatrics, Chang Gung Memorial Hospital, Taoyuan 33305, Taiwan
d Department of Materials Science and Engineering, National Taiwan University, Taipei 10617, Taiwan

ABSTRACT

Perovskite solar cell is a novel photovoltaic technology with the superior progress in efficiency and the simple solution processes. Develop lead-free or lead-reduced perovskite materials is a significant concern for high-performance perovskite solar cell. Among the alkaline earth metals, the Sr^{2+} and Ba^{2+} are suitable for Pb^{2+} replacement in perovskite film due to fitting Goldschmidt's tolerance factor. In this study, we adopted Ba-doped and Sr-doped perovskite structured materials with different doping levels, including 1.0, 5.0, and 10.0 mol%, to prepare perovskite solar cells. Both Ba-doped and Sr-doped perovskite structured materials have a related tendency in absorption behavior and surface morphology. At 10.0 mol% doping level, the power conversion efficiency (PCE) of Sr-doped perovskite solar cells is only ~0.5%, but the PCE of Ba-doped perovskite solar cells can be achieved to ~9.7%. Ba-doped perovskite solar cells showed the acceptable photovoltaic characteristics than Sr-doped perovskite solar cells. Ba dopant can partially replace the amount of lead in the perovskite solar cells, and it could be a potential candidate in the field of lead-free or lead-reduced perovskite energy materials.

© 2017 Elsevier B.V. All rights reserved.

1. Introduction

Recently, perovskite solar cell has attracted a lot of attention that make it become one of the promising solar power technology, because of its high power conversion efficiency (PCE), low production cost, and easy fabrication process. Miyasaka *et al.* first published the study about developing perovskite solar cell with a PCE of 3.8% [1]. Moreover, Miyasaka and Snaith *et al.* further used the mixed halide perovskite (i.e. $CH_3NH_3PbI_2Cl$) to obtain an increased PCE to 10.9% [2]. After that, many research groups devoted to studying perovskite solar cells and enhanced the PCE to 22.1% at present [3–5]. Perovskite structured materials could be the potential material in the emerging photovoltaic field due to its rapid PCE improvement. The common chemical formula for perovskite compounds is ABX_3, where "A" and "B" are two cations. Moreover, ABX_3 needs to be a six coordination number element to form octahedron as BX_6. The ratio of ionic radius between A and B is the major factor in forming perovskite structure. The octahedrons connect with each other by element X. Every eight octahedrons form a space where A cation is located. The ratio of ionic radius between A and B is calculated by tolerance factor. Tolerance factor between 0.9 and 1.0 leads to form cubic perovskite structure. Tolerance factor between 0.7 and 0.9 leads to form orthorhombic, rhombohedral or tetragonal perovskite structure [6]. Although perovskite-structured materials show the high PCE characteristics, it still has some challenges need to overcome, such as surface morphology roughness [7–9], difficult fabricating in air environment [10], electron–hole transportation [11–13], crystal status [14–16], and charge carrier life time [17,18]. High lead concentration is harmful to human and environment. The lead built up in the body causes serious health problems such as headache, reduced sensations, aggressive behavior, difficulty sleeping, abdominal pain, and anemia [19–21]. To overcome this problem, one of the solutions is to develop the lead-free or lead-reduced perovskite structured materials.

Many types of metal ions were used to replace the Pb^{2+} to synthesize various metal-doped perovskite compounds, including Bi^{3+}, Sn^{2+}, Ca^{2+}, Cu^{2+}, Na^+, and K^+. Miyasaka *et al.* reported the research of lead-free Bi perovskite solar cell. They successfully synthesized lead-free perovskite solar cell by replacing Pb^{2+} with Bi^{3+}. Because

* Corresponding author at: Department of Chemical and Materials Engineering, Chang Gung University, Taoyuan 33302, Taiwan. Tel.: +886 3 2118800x3545; fax: +886 3 3775580.
E-mail address: mingchungwu@mail.cgu.edu.tw (M.-C. Wu).

of the charge difference between Pb^{2+} and Bi^{3+}, the chemical formula of perovskite changed from ABX_3 to $A_3B_2X_9$ [22,23]. The highest PCE of lead-free Bi-based perovskite solar cell only showed 1.09% [24]. Navas *et al.* reported that Ca doping may cause perovskite structure changed from tetragonal crystal system to cubic crystal system [25]. In addition, many researchers focused on Sn-doped perovskite solar cells due to no lead existence. In 2014, Hao *et al.* studied Sn-based perovskite solar cell, and the results showed that the UV–vis spectra significant shifted from 800 to 1000 nm and its narrow band is ~1.1 eV. However, the PCE of Sn-based perovskite solar cell is still not higher than the Pb-based perovskite solar cell [26]. Hao *et al.* reported the other research at the same year. They set the lead-free Sn-based perovskite solar cell as the base and replaced iodine with bromine. The results displayed the significant enhancements of V_{OC} and FF, but J_{SC} decreased rapidly with the increasing the concentration of bromine [27]. Chang *et al.* reported a research about doping alkali metal (K and Na) into $MAPbI_3$, and both perovskite solar cells showed the high photovoltaic performance than the non-doped perovskite solar cell. The PCE of K-doped and Na-doped perovskite solar cells were improved from 12.8% to 15.3% and from 12.8% to 14.5%, respectively [28]. Jahandar *et al.* doped $CuBr_2$ into $MAPbI_3$ to enhance the photovoltaic performance, and their results showed increased short circuit current and PCE improved from 13.18% to 17.09% [29]. Pazoki *et al.* demonstrated the some alkaline-earth metals (Ca, Sr, and Ba) are the potential candidates to replace the toxic lead in perovskite structured materials due to the same charge and the similar ionic radius [30].

$MASrI_3$ and $MABaI_3$ could be a stable perovskite structure calculated by the density functional theory. Because $MASrI_3$ and $MABaI_3$ are the wide bandgap materials [30], they show the poor absorption in visible and infrared wavelengths. However, the slight doping using Sr^{2+} and Ba^{2+} in the perovskite structured materials can decrease the bandgap [31]. In this study, we developed the lead-reduced perovskite structured materials to fabricate the perovskite solar cells in the glovebox (nitrogen atmosphere, H_2O and $O_2 < 0.1$ ppm). The well-known perovskite structured material for photovoltaic application is $CH_3NH_3PbI_3$. We used Ba^{2+} or Sr^{2+} doped into $CH_3NH_3PbI_3$, because both alkaline earth metal ions are perfectly fitting the tolerance factor. The photovoltaic performance of Ba-doped perovskite solar cells is usually higher than Sr-doped perovskite solar cells. Hence, Ba-doped perovskite structured materials can replace the lead without decreasing the photovoltaic performance, so it could be a potential candidate in the field of perovskite structured energy materials.

2. Experimental details

2.1. Perovskite solution preparation

The methylammonium iodide (CH_3NH_3I, MAI) was synthesized by following literature [32]. The preparation of perovskite precursor solution was mixing MAI and lead chloride ($PbCl_2$, 99%, Acros) with mole ratio 2.6:1 in 0.5 mL dimethylformamide ($HCON(CH_3)_2$, DMF, anhydrous, 99.8%, Acros) at 39.0 wt%. Doped perovskite precursor solution was prepared by mixing MAI, lead chloride, barium iodide (BaI_2, 99%, Acros), and strontium iodide (SrI_2, 99%, Acros) depended on atomic ratio in 0.5 mL dimethylformamide.

2.2. Electron transporting layer precursor solution preparation

A 2.5 mL of ethanol (C_2H_5OH, 99.5%, Acros) was mixed with 375 μL of titanium isopropoxide ($Ti(OCH(CH_3)_2)_4$, TTIP, >97%, Acros) in a 7.0 mL sample bottle. Then, 35 μL of 2.0 M HCl was added to 2.5 mL of ethanol in another sample bottle. Subsequently, HCl solution was dropped into Ti precursor solution, and the mixed

solution was filtered by 0.2 μm PTFE filter. Finally, TiO_2 precursor solution was synthesized for preparing electron transporting layer.

2.3. Hole transporting layer precursor solution preparation

We prepared 2,2′,7,7′-tetrakis[*N*,*N*-di(4-methoxyphenyl)amino]-9,9′-spirobifluorene (spiro-OMeTAD, STAREK Scientific) solution by following steps. In the beginning, 104 mg lithium-bis-(trifluoromethanesulfonyl) imide ($C_2F_6LiNO_4S_2$, Li-TFSI, 99.95%, Aldrich) was added in 200.0 μL acetonitrile (CH_3CN, 99.5%, Acros) to prepare lithium salt solution. Then, 28.5 μL 4-tert-butylpyridine ($C_9H_{13}N$, tBP, 96%, Acros) and 17.5 μL lithium salt solution were dropped into 1.0 mL chlorobenzene (C_6H_5Cl, CB, 99.8%, Acros), and they were mixed together by heating magnetic stirrer. Finally, 80 mg spiro-OMeTAD powder was added in 1.0 mL of the mixed solution.

### 2.4. Fabrication of the perovskite solar cells

We cleaned the FTO glass by ultrasonicator using detergent for 5 min, methanol for 20 min, and isopropanol for 20 min. The TiO_2 precursor solution was spin-coated on FTO glass at 1000 rpm for 40 s followed by calcination process at 550 °C for 30 min. After that, the perovskite solution was spin-coated at 2000 rpm for 40 s in Mbraun glovebox system (nitrogen atmosphere, H_2O and $O_2 < 0.1$ ppm). Then, the spiro-OMeTAD solution was spin-coated at 4000 rpm for 30 s. Finally, the gold electrode was thermally deposited on the device surface with a shadow mask with 0.09 cm^2 active area by the thermal evaporation techniques.

2.5. Characterization

The photovoltaic characteristics of the device were analyzed under AM 1.5G sunlight (Newport-69920, 100 mW/cm^2) which was calibrated by a silicon reference solar cell with KG-5 filter and the current density-voltage (*J–V*) data was recorded by source meter (Keithley 2410). The delay time between each data plot is 10 ms. The morphology of metal-doped perovskite layers was observed by scanning electron microscope (SNE-4500M, SEC). UV–vis absorption spectra were measured by UV–vis spectrometer (V-630, Jasco). The curve was measured from 600 nm to 900 nm with 1000 nm/min scan rate. X-ray patterns were measured by X-ray diffractometer (XRD, Bruker, D2 phaser with Xflash 430, Germany). All of samples were measured from 10° to 50° with Cu$K\alpha$ beam ($\lambda = 1.54$ Å). The photoluminescence (PL) spectra were measured by a continuous-wave diode laser ($\lambda_{exe} = 440$ nm, PDLH-440-25, DongWoo Optron Co. Ltd.), and the signals were analyzed by photomultiplier tube detector system (PDS-1, DongWoo Optron Co. Ltd.). The time-resolved photoluminescence (TRPL) spectra were measured with an average power 1.0 mW plus laser and operated at 312.5 MHz under 2 μs duration time, which was used for excitation. The signals were analyzed by time-correlated single photon counting spectrometer (WELLS-001 FX, DongWoo Optron Co. Ltd.).

3. Results and discussion

The XRD patterns of Sr and Ba doped perovskite materials with different doping concentrations are shown in Fig. 1(a). We can observe that the intensity at 2θ of 14.27° which is the diffraction peak of perovskite (1 1 0) facet. The magnified XRD patterns in the range between 13.5° and 15.5° are shown in Fig. 1((b) and (c)). When Ba or Sr is doped into the perovskite-structured material, the intensity of (1 1 0) facet is decreased with increasing the doping concentration. However, Sr-doped perovskite material presented the decreased (1 1 0) facet and formed the phase transition. This result exhibited that the original tetragonal crystal structure was
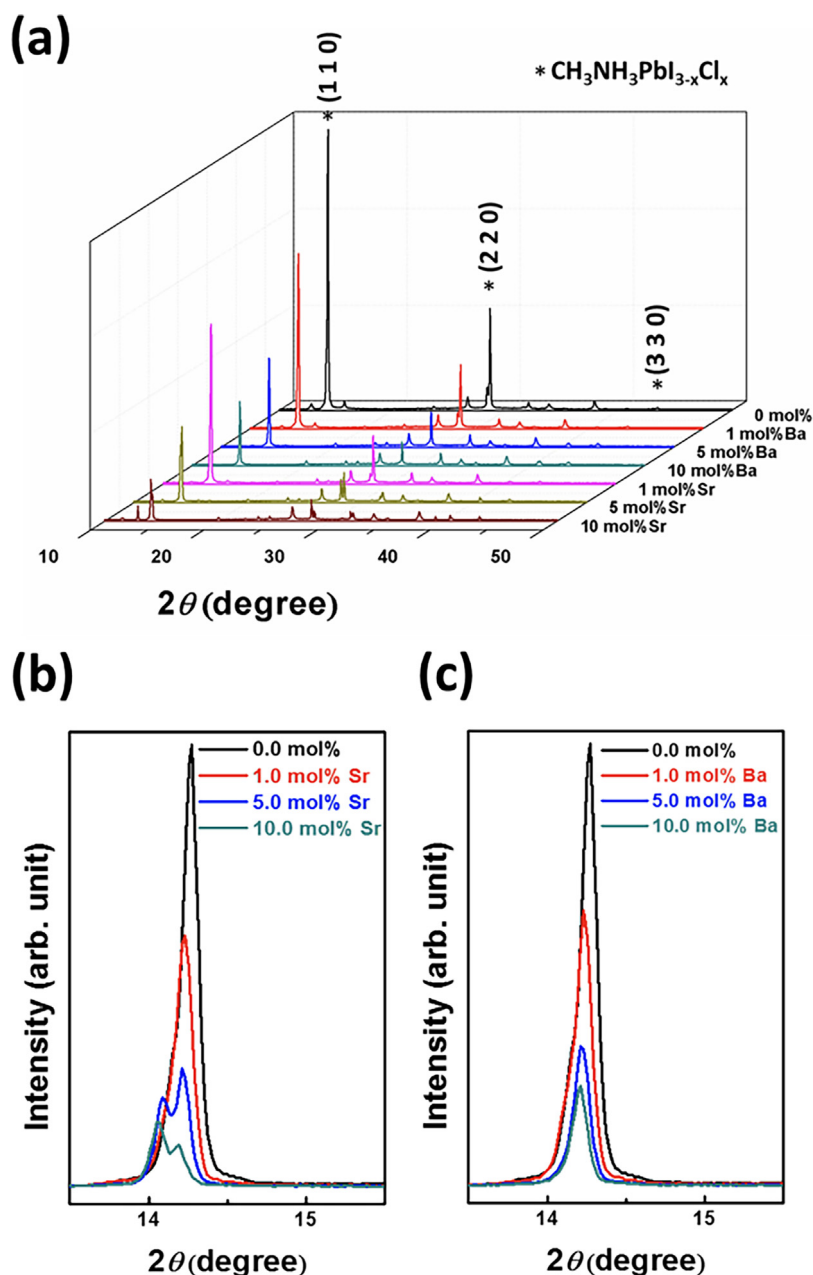
Fig. 1. (a) XRD patterns of various perovskite films with different metal doping concentrations. Magnified XRD patterns of (1 1 0) facet of various perovskite films with different doping levels, including, (b) Sr-doped perovskite films and (c) Ba-doped perovskite films.

changed by Sr^{2+} dopant (~118 pm) and formed the $MASrI_3$ [30]. In Fig. 1(c), the XRD patterns showed a slight shift to smaller diffraction angle due to the ionic radius of Ba^{2+} (~135 pm) which is larger than Pb^{2+} (~120 pm). The diffraction intensity of perovskite (1 1 0) facet is also decreased because the microstrain could reduce the crystallinity [33]. The alkaline earth metal ion dopant could distort the crystal structure of the perovskite active layer. Hence, the ionic types and radius of doping metal could cause the phase transition and crystal structure change.

Fig. 2 shows the absorption spectra of the Sr and Ba doped perovskite materials. The bandgaps of non-doped, Sr-doped (including 1.0 mol%, 5.0 mol%, and 10.0 mol%), and Ba-doped (including 1.0 mol%, 5.0 mol% and 10.0 mol%) perovskite layers are 1.56, 1.52, 1.51, 1.37, 1.53, 1.50 and 1.42, respectively. UV–vis spectra of Sr-doped (Fig. 2(a)) and Ba-doped (Fig. 2(b)) perovskite films showed the red-shift with increasing doping concentrations, because the

metal dopant in perovskite changed the electronic structure and modified the interaction with the ions in the network [25].

The SEM images of Sr and Ba-doped perovskite films with different doping concentrations are shown in Fig. 3. The pristine perovskite film (Fig. 3(a)) is as a reference to compare with Sr and Ba-doped perovskite films. The Sr-doped perovskite films (Fig. 3(b)–(d)) showed the rough surface and presented pinholes and voids, so that the crystallinity was reduced. On the other hand, the formation of $MASrI_3$ could affect the surface topography of active layer. Moreover, the sizes of pinholes and voids increased as Sr doping level increased. The surface morphologies of metal-doped perovskite film became rough with ascending doping concentration. The rough surface could cause the increasing of light scattering (Fig. 2) [34]. However, Ba-doped perovskite film exhibited smoother surface morphology than Sr-doped perovskite film, because the crystallinity of Ba-doped perovskite film is higher
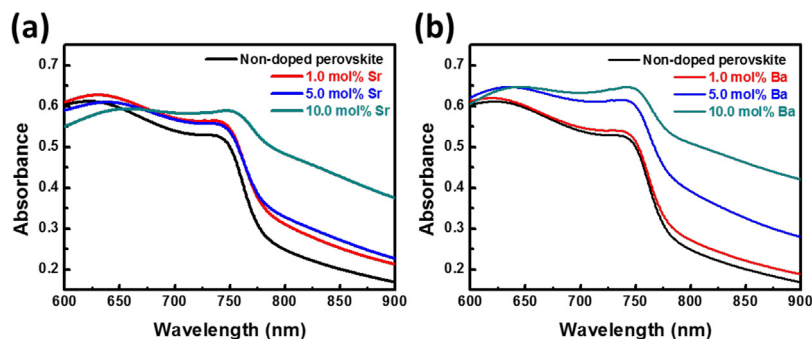
Fig. 2. UV–vis absorption spectra of (a) Sr-doped and (b) Ba-doped perovskite films with different doping concentrations.
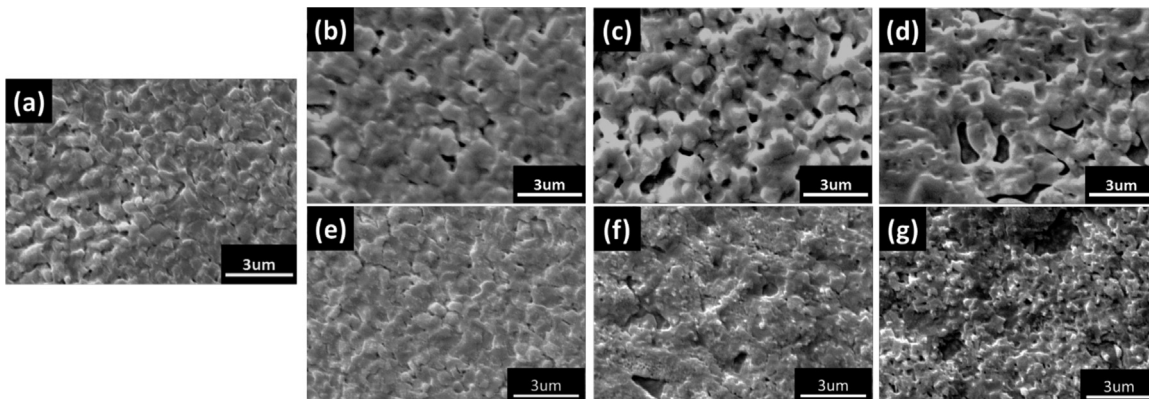

Fig. 3. SEM images of various perovskite films: (a) non-doped perovskite films, (b) and (c) Sr-doped perovskite films with 1.0 mol%, 5.0 mol%, and 10.0 mol%. (e)–(g) Ba-doped perovskite films with 1.0 mol%, 5.0 mol%, and 10.0 mol%.
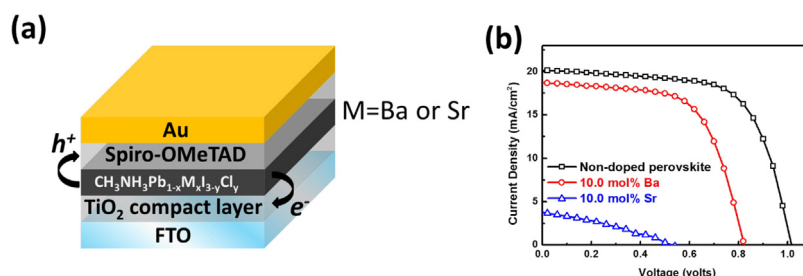

Fig. 4. (a) The schematic diagram of our perovskite solar cell structure. (b) J–V curves of the various perovskite solar cells, including non-doped perovskite solar cell, 10.0 mol% Sr-doped perovskite solar cell, and 10.0 mol% Ba-doped perovskite solar cell.

than that of Sr-doped perovskite film. The surface morphology is the key factor to affect the electron–hole transporting rate and electron–hole recombination behavior. The electron–hole transporting rate and electron–hole recombination behavior are the important issues to influence the photovoltaic performance.

The Sr-doped or Ba-doped perovskite films were used as the active layers of perovskite solar cell. The schematic diagram of metal-doped perovskite solar cell is FTO/TiO$_2$ compact layer/metal-doped perovskite/spiro-OMeTAD/Au electrode, as shown in Fig. 4(a). The J–V curves and performance of perovskite solar cells fabricated by 10.0 mol% Sr-doped and Ba-doped perovskite active layers are shown in Fig. 4(b) and Table 1, respectively. The non-doped perovskite solar cell showed 1.02 V of V_{OC}, 19.9 mA/cm^2 of J_{SC}, 67.5% of FF, and 13.7% of PCE. When Sr^{2+} or Ba^{2+} was doped into the perovskite film, the performances of solar cell decreased with increasing doping levels. Fig. 5 exhibited the photovoltaic characteristics of our perovskite solar cell. For Sr-doped perovskite

solar cells, V_{OC} (Fig. 5(a)) and FF (Fig. 5(c)) decreased extremely due to the optical bandgap, poor morphology, and reduced crystallinity. However, Ba-doped perovskite solar cells demonstrated the stable J_{SC} with increasing doping levels (Fig. 5(b)). The J_{SC} of 10.0 mol% Ba-doped perovskite solar cells was still as high as 18.8 mA/cm^2, but the J_{SC} decreased to 3.1 mA/cm^2 for 10.0 mol% Sr-doped perovskite solar cells. Ba-doped perovskite film could be more stable than Sr-doped perovskite film (Fig. 1(c)). The V_{OC} of metal-doped perovskite solar cells is related to the bandgap position of perovskite-structured materials. The bandgap decreased when doping concentration raised. The HOMO of metal-doped perovskite layer could raise to reduce V_{OC}. The 9.7% of PCE for 10.0 mol% Ba-doped perovskite solar cell is higher than 0.5% of PCE for 10.0 mol% Sr-doped perovskite solar cells (Fig. 5(d)). Thus, Ba^{2+} could be a good candidate to replace Pb^{2+} in perovskite active layer. In order to check the hysteresis, the J–V curves and photovoltaic performance of perovskite solar cell under forward and reverse

Table 1
Characteristics of Sr and Ba-doped perovskite solar cells with different doping levels.

Material	M/M + Pb (%)	V_{OC} (V)	J_{SC} (mA/cm^2)	FF (%)	PCE (%)
$CH_3NH_3PbI_{3-X}Cl_X$	0.0	1.02 ± 0.02	19.9 ± 0.4	67.5 ± 2.7	13.7 ± 0.8
$CH_3NH_3Pb_{0.99}Sr_{0.01}I_{3-X}Cl_X$	1.0	0.90 ± 0.04	17.3 ± 1.7	66.1 ± 2.5	10.3 ± 1.3
$CH_3NH_3Pb_{0.95}Sr_{0.05}I_{3-X}Cl_X$	5.0	0.77 ± 0.05	16.4 ± 2.3	62.6 ± 4.5	8.0 ± 1.0
$CH_3NH_3Pb_{0.90}Sr_{0.10}I_{3-X}Cl_X$	10.0	0.51 ± 0.17	3.1 ± 0.8	34.0 ± 3.9	0.5 ± 0.1
$CH_3NH_3Pb_{0.99}Ba_{0.01}I_{3-X}Cl_X$	1.0	0.98 ± 0.02	19.6 ± 0.5	67.8 ± 0.2	13.0 ± 0.2
$CH_3NH_3Pb_{0.95}Ba_{0.05}I_{3-X}Cl_X$	5.0	0.93 ± 0.05	19.5 ± 0.3	63.7 ± 2.7	11.6 ± 0.9
$CH_3NH_3Pb_{0.90}Ba_{0.10}I_{3-X}Cl_X$	10.0	0.85 ± 0.06	18.8 ± 0.3	60.4 ± 4.6	9.7 ± 1.2
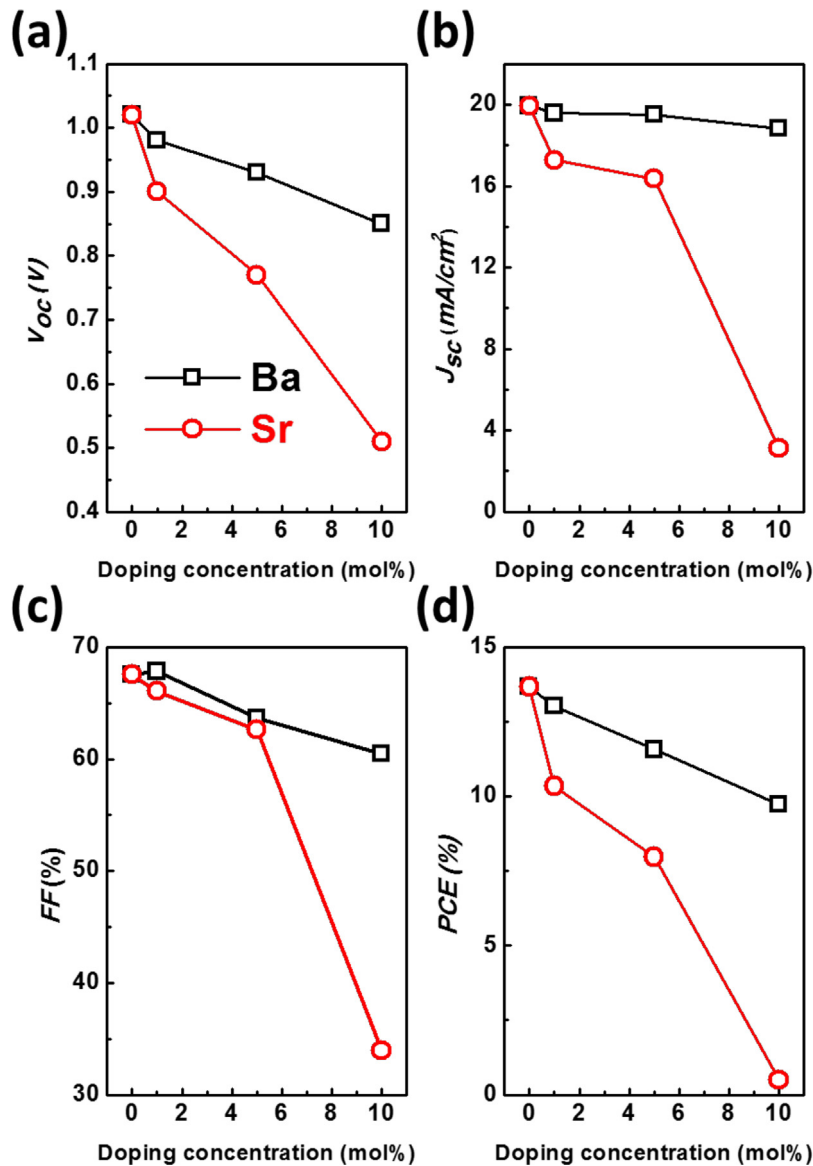
Fig. 5. Photovoltaic characteristics of Sr and Ba-doped perovskite solar cells, including (a) the open circuit current voltage, (b) the short circuit current density, (c) the fill factor, and (d) the power conversion efficiency.

scan are shown in Fig. S1 and Table S1. The hysteresis index (HI) is defined by the following equation [35]:

$$\text{Hysteresis index (HI)} = \frac{J_{RS}(0.8V_{oc}) - J_{FS}(0.8V_{oc})}{J_{RS}(0.8V_{oc})} \quad (1)$$

As expected, 0.27 of HI for 10.0 mol% Ba-doped perovskite solar cell is lower than 0.87 of HI for 10.0 mol% Sr-doped perovskite solar cell. The Ba-doped perovskite solar cell exhibits lower HI than Sr-doped perovskite solar cell due to its high crystallinity (Fig. 1). The J–V hysteresis depends on the crystallinity of perovskite film [36].

We further discussed the charge carrier dynamics of non-doped, 10.0 mol% Sr and 10.0 mol% Ba-doped perovskite films. The charge carrier dynamics of perovskite device were investigated by using PL spectrometer and TRPL set-up. The PL spectra are shown in Fig. 6(a). The non-doped perovskite film showed the highest PL quenching resulted from lower electron–hole recombination for transferring the charge effectively. The PL quenching behavior of 10.0 mol% Ba-doped perovskite film is larger than that of Sr-doped perovskite film. The topography of Ba-doped perovskite film
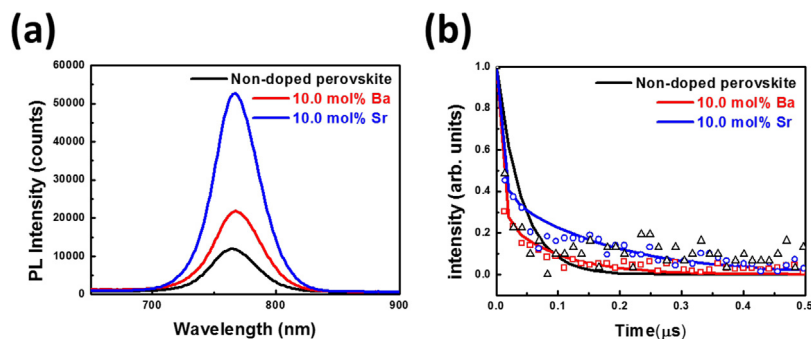
Fig. 6. Photoluminescence spectra using (a) static and (b) time-resolved of Sr and Ba-doped perovskite/TiO$_2$/FTO measured at room temperature.

Table 2
Summary of measured fast decay time (τ_1), slow decay time (τ_2), and PL average decay (τ_{avg}) for the non-doped, Sr-doped, and Ba-doped perovskite film.

Material	A_1 (%)	τ_1 (ns)	A_2 (%)	τ_2 (ns)	τ_{avg} (ns)
Non-doped perovskite layer	30.9	57.4	69.1	217.0	167.7
10.0 mol% Sr-doped perovskite layer	59.0	4.8	41.0	74.9	33.5
10.0 mol% Ba-doped perovskite layer	76.5	1.6	23.5	90.8	22.6

showed the smooth surface than Sr-doped perovskite film. The smooth morphology could improve the charge transfer behavior. We also measured the time-resolved PL spectra of various perovskite films (Fig. 6(b)). The time-resolved PL decay curve can be fitted by a bi-exponential decay function as follows:

$$F(t) = A_1 \exp\left(-\frac{t}{\tau_1}\right) + A_2 \exp\left(-\frac{t}{\tau_2}\right) \tag{2}$$

where A_1 and A_2 are amplitude fraction, respectively. τ_1 and τ_2 are fast decay time and slow decay time, respectively. The average decay lifetime was calculated by the following equation:

$$\tau_{avg} = \frac{\Sigma_i A_i \tau_i}{\Sigma_i A_i} \tag{3}$$

The measured A_1, A_2, τ_1, τ_2, and τ_{avg} for various perovskite films are listed in Table 2.

For the non-doped perovskite film, the fast decay time was 57.4 ns, the slow decay lifetime was 217.0 ns and the amplitudes were 30.9% and 69.1%, respectively. The τ_{avg} of non-doped perovskite film was 167.7 ns. For 10.0 mol% Ba-doped perovskite films, its τ_{avg} was decreased to 22.6 ns compared with 33.5 ns of 10.0 mol% Sr-doped perovskite films. Moreover, the fast decay amplitudes are increased to 76.5 ns. These results indicate that the 10.0 mol% Ba-doped perovskite could improve the electron transfer behavior from perovskite active layer to TiO$_2$ electron transporting layer. Hence, the PL intensity of Ba-doped perovskite film was lower than Sr-doped perovskite film (Fig. 6(a)). The lower PL intensity means the less electron–hole recombination. The PL spectra and time-resolved PL results presented the great influence to PCE of perovskite solar cells. Moreover, the PCE of Ba-doped perovskite solar cell is much higher than Sr-doped perovskite solar cell (Fig. 4(b)).

4. Conclusion

In summary, various concentration of Ba-doped and Sr-doped perovskite solar cell are successfully prepared. Both Ba-doped and Sr-doped perovskite films displayed the similar tendency of optical absorption and surface morphology. We compared both metal-doped perovskite solar cell at 1.0, 5.0, 10.0 mol% doping concentration. Both Ba-doped and Sr-doped perovskite solar cells led to the decreased photovoltaic characteristic with increasing doping concentration. Ba-doped perovskite solar cell usually exhibited high performance compared with Sr-doped perovskite solar cell.

At 10 mol% Ba doping concentration, Ba-doped perovskite solar cell had 9.72% of PCE and Sr-doped perovskite solar cell had just 0.5% of PCE. We found that Ba is the nice choice for lead-reduced perovskite solar cells. Although the metal-doped perovskite solar cell had less PCE than non-doped one, Ba doping still has a great prospect for metal-doped and lead-free perovskite solar cell research area.

Appendix A. Supplementary data

Supplementary data associated with this article can be found, in the online version, at http://dx.doi.org/10.1016/j.apsusc.2017.08.131.

References

[1] A. Kojima, K. Teshima, Y. Shirai, T. Miyasaka, Organometal halide perovskites as visible-light sensitizers for photovoltaic cells, J. Am. Chem. Soc. 131 (2009) 6050–6051.
[2] M.M. Lee, J. Teuscher, T. Miyasaka, T.N. Murakami, H.J. Snaith, Efficient hybrid solar cells based on meso-superstructured organometal halide perovskites, Science 338 (2012) 643–647.
[3] J.H. Heo, M.S. You, M.H. Chang, W. Yin, T.K. Ahn, S.-J. Lee, S.-J. Sung, D.H. Kim, S.H. Im, Hysteresis-less mesoscopic CH$_3$NH$_3$PbI$_3$ perovskite hybrid solar cells by introduction of Li-treated TiO$_2$ electrode, Nano Energy 15 (2015) 530–539.
[4] K.N. Elumalai, A.M. Mahmud, D. Wang, A. Uddin, Perovskite solar cells: progress and advancements, Energies 9 (2016) 861.
[5] F. Behrouznejad, S. Shahbazi, N. Taghavinia, H.-P. Wu, E. Wei-Guang Diau, A study on utilizing different metals as the back contact of CH$_3$NH$_3$PbI$_3$ perovskite solar cells, J. Mater. Chem. A 4 (2016) 13488–13498.
[6] T.J. Jacobsson, M. Pazoki, A. Hagfeldt, T. Edvinsson, Goldschmidt's rules and strontium replacement in lead halogen perovskite solar cells: theory and preliminary experiments on CH$_3$NH$_3$SrI$_3$, J. Phys. Chem. C 119 (2015) 25673–25683.
[7] C.-Y. Chang, C.-Y. Chu, Y.-C. Huang, C.-W. Huang, S.-Y. Chang, C.-A. Chen, C.-Y. Chao, W.-F. Su, Tuning perovskite morphology by polymer additive for high efficiency solar cell, ACS Appl. Mater. Interfaces 7 (2015) 4955–4961.
[8] W. Qiu, T. Merckx, M. Jaysankar, C. Masse de la Huerta, L. Rakocevic, W. Zhang, U.W. Paetzold, R. Gehlhaar, L. Froyen, J. Poortmans, D. Cheyns, H.J. Snaith, P. Heremans, Pinhole-free perovskite films for efficient solar modules, Energy Environ. Sci. 9 (2016) 484–489.
[9] Y. Zhao, J. Liu, X. Lu, Y. Gao, X. You, X. Xu, Improving the efficiency of perovskite solar cells through optimization of the CH$_3$NH$_3$PbI$_3$ film growth in solution process method, Appl. Surf. Sci. 359 (2015) 560–566.
[10] S. Pathak, A. Sepe, A. Sadhanala, F. Deschler, A. Haghighirad, N. Sakai, K.C. Goedel, S.D. Stranks, N. Noel, M. Price, S. Hüttner, N.A. Hawkins, R.H. Friend, U. Steiner, H.J. Snaith, Atmospheric Influence upon crystallization and electronic

disorder and its impact on the photophysical properties of organic–inorganic perovskite solar cells, ACS Nano 9 (2015) 2311–2320.

[11] Y. Liu, Q. Chen, H.-S. Duan, H. Zhou, Y. Yang, H. Chen, S. Luo, T.-B. Song, L. Dou, Z. Hong, Y. Yang, A dopant-free organic hole transport material for efficient planar heterojunction perovskite solar cells, J. Mater. Chem. A 3 (2015) 11940–11947.

[12] J. Choi, S. Song, M.T. Hörantner, H.J. Snaith, T. Park, Well-defined nanostructured, single-crystalline TiO_2 electron transport layer for efficient planar perovskite solar cells, ACS Nano 10 (2016) 6029–6036.

[13] T. Singh, J. Singh, T. Miyasaka, Role of metal oxide electron–transport layer modification on the stability of high performing perovskite solar cells, ChemSusChem 9 (2016) 2559–2566.

[14] G. Niu, H. Yu, J. Li, D. Wang, L. Wang, Controlled orientation of perovskite films through mixed cations toward high performance perovskite solar cells, Nano Energy 27 (2016) 87–94.

[15] C.-M. Tsai, G.-W. Wu, S. Narra, H.-M. Chang, N. Mohanta, H.-P. Wu, C.-L. Wang, E.W.-G. Diau, Control of preferred orientation with slow crystallization for carbon-based mesoscopic perovskite solar cells attaining efficiency 15%, J. Mater. Chem. A 5 (2017) 739–747.

[16] G.E. Eperon, C.E. Beck, H.J. Snaith, Cation exchange for thin film lead iodide perovskite interconversion, Mater. Horiz. 3 (2016) 63–71.

[17] E.S. Parrott, R.L. Milot, T. Stergiopoulos, H.J. Snaith, M.B. Johnston, L.M. Herz, Effect of structural phase transition on charge-carrier lifetimes and defects in $CH_3NH_3SnI_3$ perovskite, J. Phys. Chem. Lett. 7 (2016) 1321–1326.

[18] S.D. Stranks, G.E. Eperon, G. Grancini, C. Menelaou, M.J.P. Alcocer, T. Leijtens, L.M. Herz, A. Petrozza, H.J. Snaith, Electron–hole diffusion lengths exceeding 1 micrometer in an organometal trihalide perovskite absorber, Science 342 (2013) 341.

[19] ⟨http://www.who.int/mediacentre/factsheets/fs379/en/⟩.

[20] H. Needleman, Lead poisoning, Annu. Rev. Med. 55 (2004) 209–222.

[21] R.C. Gracia, W.R. Snodgrass, Lead toxicity and chelation therapy, Am. J. Health-Syst. Pharm. 64 (2006) 45.

[22] T. Singh, A. Kulkarni, M. Ikegami, T. Miyasaka, Effect of electron transporting layer on bismuth-based lead-free perovskite ($CH_3NH_3)_3Bi_2I_9$ for photovoltaic applications, ACS Appl. Mater. Interfaces 8 (2016) 14542–14547.

[23] A. Kulkarni, T. Singh, M. Ikegami, T. Miyasaka, Photovoltaic enhancement of bismuth halide hybrid perovskite by *N*-methyl pyrrolidone-assisted morphology conversion, RSC Adv. 7 (2017) 9456–9460.

[24] B.-W. Park, B. Philippe, X. Zhang, H. Rensmo, G. Boschloo, E.M.J. Johansson, Bismuth based hybrid perovskites $A_3Bi_2I_9$ (A: methylammonium or cesium) for solar cell application, Adv. Mater. 27 (2015) 6806–6813.

[25] J. Navas, A. Sanchez-Coronilla, J.J. Gallardo, N. Cruz Hernandez, J.C. Pinero, R. Alcantara, C. Fernandez-Lorenzo, D.M. De los Santos, T. Aguilar, J. Martin-Calleja, New insights into organic–inorganic hybrid perovskite $CH_3NH_3PbI_3$ nanoparticles. An experimental and theoretical study of doping in Pb^{2+} sites with Sn^{2+}, Sr^{2+}, Cd^{2+} and Ca^{2+}, Nanoscale 7 (2015) 6216–6229.

[26] F. Hao, C.C. Stoumpos, R.P.H. Chang, M.G. Kanatzidis, Anomalous band gap behavior in mixed Sn and Pb perovskites enables broadening of absorption spectrum in solar cells, J. Am. Chem. Soc. 136 (2014) 8094–8099.

[27] F. Hao, C.C. Stoumpos, D.H. Cao, R.P.H. Chang, M.G. Kanatzidis, Lead-free solid-state organic–inorganic halide perovskite solar cells, Nat. Photonics 8 (2014) 489–494.

[28] J. Chang, Z. Lin, H. Zhu, F.H. Isikgor, Q.-H. Xu, C. Zhang, Y. Hao, J. Ouyang, Enhancing the photovoltaic performance of planar heterojunction perovskite solar cells by doping the perovskite layer with alkali metal ions, J. Mater. Chem. A 4 (2016) 16546–16552.

[29] M. Jahandar, J.H. Heo, C.E. Song, K.-J. Kong, W.S. Shin, J.-C. Lee, S.H. Im, S.-J. Moon, Highly efficient metal halide substituted $CH_3NH_3I(PbI_2)_{1−X}(CuBr_2)_X$ planar perovskite solar cells, Nano Energy 27 (2016) 330–339.

[30] M. Pazoki, T.J. Jacobsson, A. Hagfeldt, G. Boschloo, T. Edvinsson, Effect of metal cation replacement on the electronic structure of metalorganic halide perovskites: replacement of lead with alkaline-earth metals, Phys. Rev. B: Condens. Matter 93 (2016) 144105.

[31] X. Shai, L. Zuo, P. Sun, P. Liao, W. Huang, E.-P. Yao, H. Li, S. Liu, Y. Shen, Y. Yang, M. Wang, Efficient planar perovskite solar cells using halide Sr-substituted Pb perovskite, Nano Energy 36 (2017) 213–222.

[32] M.-C. Wu, S.-H. Chan, M.-H. Jao, W.-F. Su, Enhanced short-circuit current density of perovskite solar cells using Zn-doped TiO_2 as electron transport layer, Sol. Energy Mater. Sol. Cells 157 (2016) 447–453.

[33] J.T.-W. Wang, Z. Wang, S. Pathak, W. Zhang, D.W. deQuilettes, F. Wisnivesky-Rocca-Rivarola, J. Huang, P.K. Nayak, J.B. Patel, H.A. Mohd Yusof, Y. Vaynzof, R. Zhu, I. Ramirez, J. Zhang, C. Ducati, C. Grovenor, M.B. Johnston, D.S. Ginger, R.J. Nicholas, H.J. Snaith, Efficient perovskite solar cells by metal ion doping, Energy Environ. Sci. 9 (2016) 2892–2901.

[34] B. Li, C. Fei, K. Zheng, X. Qu, T. Pullerits, G. Cao, J. Tian, Constructing water-resistant $CH_3NH_3PbI_3$ perovskite films via coordination interaction, J. Mater. Chem. A 4 (2016) 17018–17024.

[35] N.J. Jeon, J.H. Noh, Y.C. Kim, W.S. Yang, S. Ryu, S.I. Seok, Solvent engineering for high-performance inorganic–organic hybrid perovskite solar cells, Nat. Mater. 13 (2014) 897–903.

[36] N. Tripathi, M. Yanagida, Y. Shirai, T. Masuda, L. Han, K. Miyano, Hysteresis-free and highly stable perovskite solar cells produced via a chlorine-mediated interdiffusion method, J. Mater. Chem. A 3 (2015) 12081–12088.